Editors' Suggestion | Featured in Physics

Surpassing the Resistance Quantum with a Geometric Superinductor

M. Peruzzo,[†] A. Trioni,[†] F. Hassani, M. Zemlicka, and J. M. Fink[*]
Institute of Science and Technology Austria, Klosterneuburg 3400, Austria

(Received 31 July 2020; revised 20 August 2020; accepted 28 September 2020; published 29 October 2020)

Superinductors have a characteristic impedance exceeding the resistance quantum $R_Q \approx 6.45$ kΩ, which leads to a suppression of ground-state charge fluctuations. Applications include the realization of hardware-protected qubits for fault-tolerant quantum computing, improved coupling to small-dipole-moment objects, and the definition of a new quantum-metrology standard for the ampere. In this work, we refute the widespread notion that superinductors can only be implemented based on kinetic inductance, i.e., using disordered superconductors or Josephson-junction arrays. We present the modeling, fabrication, and characterization of 104 planar aluminum-coil resonators with a characteristic impedance up to 30.9 kΩ at 5.6 GHz and a capacitance down to ≤ 1 fF, with low loss and a power handling reaching 10^8 intracavity photons. Geometric superinductors are free of uncontrolled tunneling events and offer high reproducibility, linearity, and the ability to couple magnetically—properties that significantly broaden the scope of future quantum circuits.

DOI: 10.1103/PhysRevApplied.14.044055

I. INTRODUCTION

In recent years, the field of superconducting quantum circuits has been introduced to a new player: the superinductor [1,2]. It is defined as a circuit element with zero dc resistance and a characteristic impedance $Z_C > R_Q = h/(2e)^2 \approx 6.45$ kΩ. For many quantum applications, it needs to be initialized in its ground state, which requires a low-loss self-resonance in the gigahertz range.

Superinductor resonators affect their local quantum environment. In the ground state, a resonator's dimensionless charge and phase fluctuations are impedance dependent and their ratio is given by $\delta n/\delta\phi = R_Q/Z_C$. For this reason, superinductors have been identified as necessary to measure the dual element of the Josephson junction, the phase-slip junction [3], since the observation of locked phase-slip oscillations (dual Shapiro steps) relies on a suppression of charge fluctuations and resistive heating [4–6]. Such a measurement raises the prospect of a new quantum-metrology standard for current [7–9]. In addition, new qubits such as the fluxonium [10–12] and hardware-protected qubits [13,14] such as the 0-π [1,15–18], as well as robust quantum error-correction schemes [19], are dependent on reliable low-loss superinductors.

High-characteristic-impedance resonators with fundamental frequency f_0 and low stray capacitance C give rise to large zero-point voltage fluctuations $V_{\mathrm{ZPF}} = \sqrt{hf_0/(2C)} = 2\pi f_0\sqrt{\hbar Z_C/2}$. The use of a superinductance can therefore boost conventional coupling limits in circuit QED [20,21] and facilitate coupling to hybrid piezoelectric components [22], as well as to systems having small electric dipole moments, such as electrons in quantum dots [23] and polar molecules [24]. Microwave optomechanics experiments such as ground-state cooling [25] and wavelength conversion [26] benefit from large V_{ZPF} but also require parametric coupling, which is increased by a strong coherent drive that relies on a high degree of linearity of the inductance [27].

To date, implementations of superinductors have been based on kinetic inductance, either by fabricating Josephson-junction arrays [10,28–31] or using highly disordered materials, such as nanowires [12,32–34] or granular aluminum [11,35,36]. Geometric inductances are widely considered to be unsuitable as superinductors, since reaching $Z_C > R_Q$ has been argued to be impossible [2,10,28,36]. With a simple single-wire resonator, the characteristic impedance will indeed be bounded to approximately the impedance of free space $Z_0 = \sqrt{\mu_0/\epsilon_0} = 377$ Ω. In this paper, we exceed this limit by almost 2 orders of magnitude by making use of the mutual-inductance contribution of concentric loops in the form of a planar coil together with drastic miniaturization and substrate engineering.

II. PROOF OF CONCEPT AND MODEL

The geometric impedance of a straight wire according to the transmission-line model [37] is length independent and is defined by

$$Z_{\mathrm{wire}} = \frac{1}{\pi}\sqrt{\frac{\mu_0}{\epsilon_0\epsilon_r}}\operatorname{arccosh}(d/w), \tag{1}$$

[*]jfink@ist.ac.at
[†]These authors contributed equally to this work.

where w is the width of the wire and d is the distance to ground. One could try to increase Z_{wire} by increasing d, but once d is in the order of the wavelength, the circuit starts to radiate energy, as if it is shunted by a load resistance Z_0 at resonance [2]. However, by winding the single wire in a planar and circular spiral form, the geometric inductance is enhanced, as expressed by the current-sheet method formula [38,39]

$$L_g = \frac{\mu_0 n^2 d_{\text{av}}}{2}(\ln(2.5/\rho) + 0.2\rho^2), \tag{2}$$

where μ_0 is the vacuum permeability (assuming that none of the materials have magnetic properties), n is the number of turns, $d_{\text{av}} = \frac{d_{\text{in}}+d_{\text{out}}}{2}$ is the average between the inner and the outer diameter of the coil, and $\rho = (d_{\text{out}} - d_{\text{in}})/(d_{\text{out}} + d_{\text{in}})$ is the fill ratio of the coil, which for our geometries is close to unity. As d_{out} is linear in the number of turns, Eq. (2) shows that the geometric inductance increases as $L_g \sim n^3$.

From the analytical model in Ref. [40], an expression for the fundamental resonance of a planar circular coil can be calculated as

$$f_g = \xi \frac{c_0}{\sqrt{\epsilon_{\text{eff}}}} \frac{2p}{\pi (d_{\text{in}} + 2np)^2}, \tag{3}$$

where ξ is a shape-dependent constant (for circular coils, $\xi = 0.81$), the pitch p is the distance between adjacent turns (the wire width plus spacing), ϵ_{eff} is the effective relative permittivity, n is the number of turns, and c_0 is the speed of light in vacuum. Equation (3) is based on purely geometric considerations that are valid for $n \gg 1$ and $\rho \approx 1$ and it shows the resonance scaling as $f_g \sim n^{-2}p^{-1} \sim l^{-1}$ [41], where l is the wire length, similar to a distributed-element resonator. Modeling the coil as a simple LC oscillator, we can express the impedance as $Z_C = \sqrt{L/C} = 2\pi f_0 L$ and conclude that the characteristic impedance scales with the number of turns $Z_C \sim n$ and that the parasitic capacitance of the inductor is linear in the coil radius $C \sim np$.

The favorable scaling of the impedance and resonance of a coil with respect to a straight wire can be seen in Fig. 1(a). While the frequency of the wire ($f_0 = c_0/2l$) and the coil [Eq. (3)] scale similarly with respect to length, the impedance of the coil is increasing as $Z_C = 2\pi f_g L_g \sim \sqrt{l}/p$. The plot shows that the theoretical limit that constrains the characteristic impedance of the straight wire is lifted for the coil and that the superinductor regime is attainable with a fundamental frequency in the gigahertz range.

Figure 1(b) highlights the distributed-element behavior of the coil resonator. It displays the current distribution of a coil as a function of radius r taken from a finite-element-method (FEM) simulation and that of a $\lambda/2$ resonator $I(r) = I_0 \sin[\pi(2r/d_{\text{out}})^2]$ [40], which neglects mutual inductance between turns.

Figure 1(c) compares the simulated frequency-dependent admittance of a coil shunted with a single lumped port and that of a simple LC circuit $Y(f) = i2\pi fC + 1/(i2\pi fL)$. The first zero crossing represents the fundamental frequency of the coil. The capacitance can be extracted [42] by taking the derivative of the imaginary part of the admittance at that frequency, $C = (1/4\pi)(d/df)\text{Im}(Y)|_{f=f_0}$, and we find that the resulting inductance $L_g = 1/[C(2\pi f_0)^2] \approx 163$ nH is consistent with Eq. (2), for the same coil, i.e., $L_g \approx 173$ nH. We obtain a similar agreement, i.e., $L_g \approx 180$ nH, by extracting f_0 and its derivative df_0/dC from the simulated S_{11} parameter of a weakly coupled wave port,

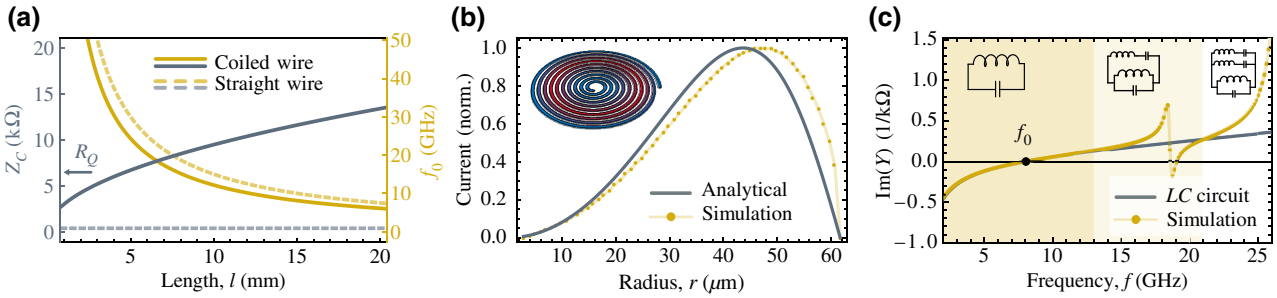

FIG. 1. (a) An analytical comparison of the characteristic impedance (blue) and first resonance frequency (yellow) for a straight wire ($d/w = 10$, dashed) and a coil ($p = 1$ μm, $\rho = 1$, solid) in vacuum ($\epsilon_{\text{eff}} = 1$). While the mutual inductance of the coil allows for an impedance increase with length, it only reduces the resonance frequency by a constant factor. (b) The normalized current distribution for a coil with $p = 1$ μm, $n = 60$, and $d_{\text{in}} = 6$ μm. The simulated points (yellow, the line is a guide to the eye) follow approximately the analytical model for a $\lambda/2$ resonator (blue). The inset shows the current-amplitude distribution, where red corresponds to high current values and blue to low values. (c) The admittance-frequency response for the same coil in vacuum. The yellow dots are obtained from FEM simulations. The zero crossing (black dot) represents the first resonance frequency. The blue line is the admittance for a LC circuit, in agreement with the simulated data at low frequencies (dark yellow area). Above, Y displays additional resonances, which can be taken into account with the equivalent circuits shown in the insets. The coil resonator can be modeled as an LC circuit around f_0, below which it behaves as a pure inductor.

in direct analogy to the experimental situation shown in Fig. 2(b).

The two admittance curves in Fig. 1(c) match in the dark shaded area, beyond which adding more LC series circuits to the model increases the accuracy up to the desired frequency (see the insets). This certifies that one can consider the coil as an ideal LC oscillator with a characteristic impedance of Z_C up to and beyond its first resonance. Furthermore, below its fundamental frequency, the coil has a negative imaginary admittance, making it an ideal inductor. The assertions made in the rest of this paper will pertain only to the frequency region in which the LC approximation is valid.

III. DESIGN AND FABRICATION

It follows from Eqs. (2) and (3) and the relation $Z_C = 2\pi f_0 L$ that the characteristic impedance of a coil can be made larger than R_Q simply by adding turns; this, however, decreases f_0, which scales as l^{-1}. In order to keep the self-resonance in the gigahertz regime, we rely on two tactics. First, we reduce the pitch to maximize the turn-number-to-length ratio and therefore the characteristic impedance per unit length. Second, we reduce the ϵ_{eff} of the substrate, which lowers the capacitance without affecting the inductance of the coil.

Regarding the second point, we fabricate coils formed by an evaporated 100-nm-thick aluminum wire, as shown in Figs. 2(a)–2(c), on three different substrates, i.e., (i) high-resistivity silicon (Si), (ii) 220-nm silicon membrane separated from a silicon handle wafer by 3 μm of vacuum (silicon on insulator, SOI), and (iii) a fully suspended 220-nm silicon membrane (SOI back-etched, SOI-BE) (for details, see Appendix A). For each substrate, we fabricate several coils with different n and p values and measure their f_0, internal (Q_i), and external (Q_e) quality factors in a dilution refrigerator, as shown in Fig. 2(d) and further discussed in Appendix B.

IV. LOSS, LINEARITY, AND KINETIC INDUCTANCE

We characterize a reference device on SOI-BE with a pitch of 300 nm, 155 turns, a first resonance at 4.55 GHz, and a geometric inductance of 933.9 nH. It is an average Q_i device for the SOI-BE coils that are measured with additional radiation shielding, a comparably high $Q_e \approx 10^5$, and an optimized vapor-hydrofluoric-acid (VHF) release. Figure 3(a) shows the typical dependence of Q_i as a function of the intraresonator photon number n_P. From the fit to a two-level-system (TLS) model (for details, see Appendix C), we extract an effective-loss tangent $F \cdot \delta_{\text{TLS}} = 1.3 \times 10^{-5}$. The best device with $p = 200$ nm shows about 10 times lower loss, on a par with state-of-the-art millimeter-sized coplanar waveguide resonators on sapphire [43]. Generally speaking, for stronger waveguide coupling, we

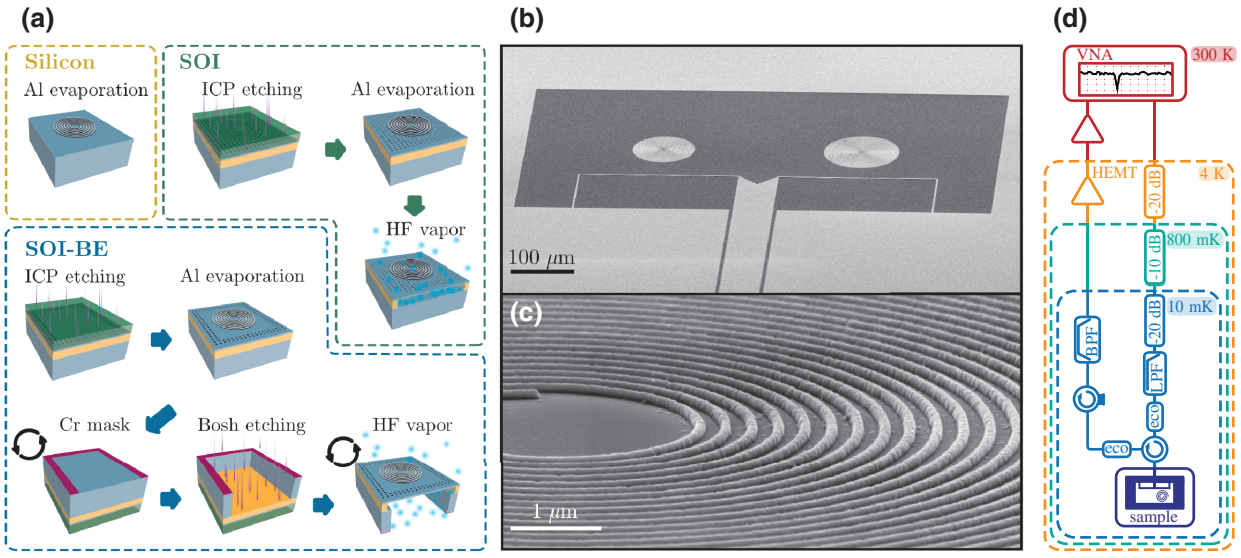

FIG. 2. (a) The main nanofabrication steps for each substrate (for details, see Appendix A). (b) A scanning-electron-microscopy image of the coil resonators inductively coupled to the shorted coplanar waveguide feed line. (c) An enlarged view of an aluminum-coil resonator with pitch 300 nm on SOI-BE. (d) A schematic of the measurement setup. The sample is bonded to a printed circuit board, mounted in a copper sample box and cooled down to 10 mK in a cryogenic dilution refrigerator. It is shielded by two magnetic shields and a radiation shield. The incoming signal from the vector-network analyzer (VNA) is attenuated by approximately 82 dB (considering attenuators and cable losses) and passes through one low-pass filter (LPF) and a circulator. Two ECCOSORB filters are attached to the input and output of the circulator. The outbound signal passes through another circulator for isolation and a band-pass filter (BPF) before being amplified by a low-temperature amplifier (HEMT) and further room-temperature amplifiers.

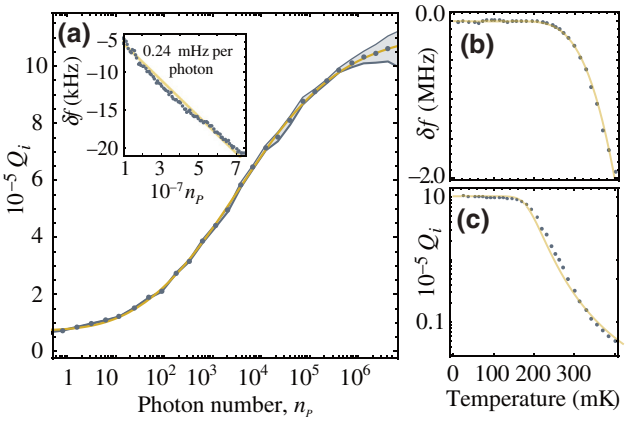

FIG. 3. (a) The measured Q_i of a representative overcoupled coil ($p = 300$ nm, $n = 155$, $Q_e = 6 \times 10^4$ on SOI-BE) as a function of the mean intraresonator photon number n_P. The blue dots are values extracted from a Lorentzian fit and the band represents the 90% confidence interval. The yellow line is a fit to a TLS model. The inset shows the frequency shift $\delta f = 0.24$ mHz per photon, obtained from a linear fit (yellow) of the measured data (blue dots). (b),(c) The blue dots are measured values for the same device as in (a). The yellow lines represent the fits to a BCS model, which yields $L_k = 58.0$ nH.

observe lower values of Q_i. However, for $Q_e \geq 5 \times 10^4$, the high power Q_i is consistently above 10^6. The full range of values can be found in Table I.

The inset in Fig. 3(a) shows the degree of nonlinearity of the resonance. From a linear fit, we extract a frequency shift of $\delta f = f_0(n_P) - f_0(0) = 0.24$ mHz per photon. At even higher powers, typically $10^6 < n_P < 10^8$, the Lorentzian shape of the resonance starts to distort, indicating the onset of a breakdown of superconductivity.

In order to quantify the effect of kinetic inductance, we perform temperature sweeps on the same device. Figures 3(b) and 3(c) show its frequency shift $\delta f\,(T) = f_0(T) - f_0(0)$ and quality-factor degradation $\delta Q_i^{-1}(T) = Q_i^{-1}(T) - Q_i^{-1}(0)$ as a function of the temperature T. This behavior can be accurately modeled using Mattis-Bardeen equations (see Appendix C). We extract a value of $L_k = 58.0$ nH, i.e., only 5.9% of the total L. From this value and the equation [44]

$$L_k = \mu_0 \lambda_L^2(0) \frac{l}{wh}, \tag{4}$$

we infer a London penetration depth $\lambda_L(0)$ of 147 nm, where μ_0 is the vacuum permeability and l, w, and h are the length, width, and thickness of the wire. This number is henceforth used to estimate the small correction due to kinetic inductance for all coils.

V. CHARACTERISTIC IMPEDANCE AND CAPACITANCE

Figure 4 summarizes the data extracted from 104 different coils on three substrates. The first row shows the measured frequency data as a function of the number of turns n for each substrate. The fits (lines) are taken from Eq. (3) with a correction to include the kinetic inductance

$$f_0 = f_g \sqrt{\frac{L_g}{L_g + L_k}}, \tag{5}$$

where the only fit parameter is the effective permittivity ϵ_{eff} in f_g. The second row in Fig. 4 shows the characteristic impedance obtained with $Z_C = 2\pi f_0 (L_g + L_k)$, where L_g and L_k are calculated using Eqs. (2) and (4) and the

TABLE I. A parameter summary of the measured geometric superinductor resonators. The f_0 values are from measurements. The L_g and L_k values are from Eqs. (2) and (4) of the main text, respectively. The C and Z_C values are calculated assuming the LC behavior. The Q_i^{low} and Q_i^{high} values are from the fundamental resonance fit at low and high intraresonator photon numbers. The underlined values refer to devices measured with additional radiation shielding, weaker coupling strengths (high Q_e), and optimized VHF release resulting in a higher Q_i, as discussed in Appendix B.

Substrate	p (μm)	Diameter (μm)	f_0 (GHz)	L_g (nH)	L_k (nH)	C (fF)	Z_C (kΩ)	V_{ZPF} (μV)	Q_i^{low} ($\times 10^5$)	Q_i^{high} ($\times 10^5$)
Silicon	1	72–90	10.94–7.00	32.04–62.90	2.71–4.27	6.09–7.71	2.39–2.95	24.39–17.34	0.70–1.70	1.93–15.4
	0.5	47–60	12.05–7.73	35.85–74.77	4.66–7.62	4.30–5.15	2.89–3.81	30.46–22.30	0.26–1.44	3.04–17.5
	0.3	36.6–63	12.12–4.17	47.15–240.68	7.88–23.46	3.13–5.53	4.19–6.91	35.80–15.80	0.36–6.06	0.71–50.0
SOI	1	86–118	12.47–6.48	55.08–142.34	3.92–7.40	2.76–4.03	4.62–6.09	38.67–23.08	0.05–1.08	0.33–30.2
	0.5	63–82	13.57–7.76	86.47–190.97	8.39–14.26	1.45–2.05	8.09–10.01	55.69–35.43	0.12–1.15	0.18–5.51
	0.3	49.2–66	14.52–7.80	113.97–276.27	14.13–25.59	0.94–1.38	11.68–14.80	71.59–43.31	0.02–0.37	0.22–0.82
SOI-BE	1	102–130	11.71–7.31	91.93–190.32	5.53–8.99	1.90–2.38	7.17–9.15	45.22–31.88	0.16–0.51	0.20–0.92
	0.5	74–88	11.53–8.36	140.29–236.08	11.60–16.44	1.25–1.43	11.00–13.27	55.17–43.95	0.08–0.71	0.27–1.73
	0.3	59.4–99	11.39–4.55	201.19–933.91	20.69–57.85	0.88–1.23	15.88–28.38	65.49–35.01	0.04–0.17	0.10–0.35
									0.24–1.66	1.11–10.9
	0.2	62–72	7.09–5.61	515.00–807.51	50.76–68.62	0.89–0.92	25.22–30.89	51.41–44.99	1.57–7.51	4.67–21.4

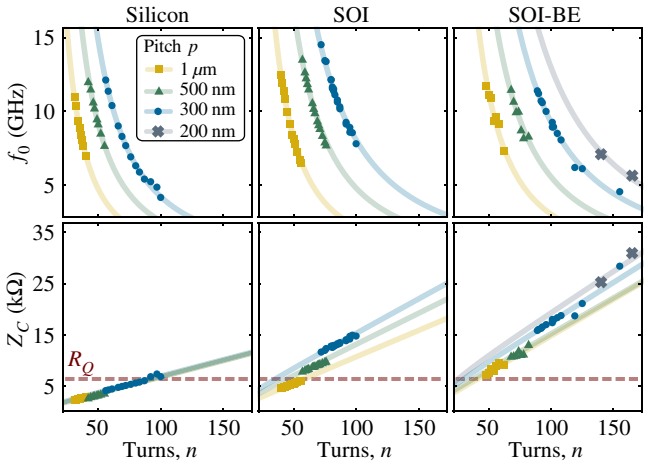

FIG. 4. The first row shows all measured resonance frequencies for coils with different pitches on the three different substrates. The data follow the trend of Eq. (5), with ϵ_{eff} as the only fit parameter. The second row represents the characteristic impedances calculated using the formula $Z_C = 2\pi f_0(L_g + L_k)$, where f_0 is the measured resonance frequency of each coil and L_g and L_k are from Eqs. (2) and (4), respectively. The lines are deduced from the corresponding fit in the first row. While it is possible to surpass R_Q on silicon, lower-permittivity substrates allow for significantly higher frequencies.

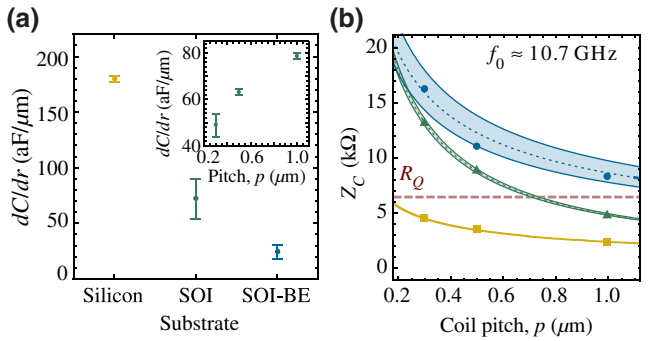

FIG. 5. (a) The extracted capacitance per unit radius for three different substrates. The dots represent the average capacitance that would be added by increasing the radius of the coil by 1 μm. The larger error bar for SOI results from the pitch dependence shown in the inset. (b) The inferred scaling of the characteristic impedance as a function of the pitch at a fixed frequency of $f_0 \approx$ 10.7 GHz. The dashed lines indicate the impedance scaling for each substrate (silicon in yellow, SOI in green, SOI-BE in blue) considering the average ϵ_{eff} value extracted from the fits in Fig. 4. The bands account for the permittivity uncertainty from the fit. For SOI, the strong pitch dependence of ϵ_{eff} is taken into account with a quadratic interpolation.

frequency f_0 is given by the data (points) and the fits to the data (lines) shown in the first row. The fits are in excellent agreement with the data points and we find ϵ_{eff} values of 6.89 ± 0.09 for silicon, 2.04 ± 0.93 for SOI, and 1.25 ± 0.19 for SOI-BE. In the case of silicon, ϵ_{eff} can be estimated with $\epsilon_{\text{eff}} = (\epsilon_{\text{Si}} + 1)/2 = 6.5$, very close to the fit results, and in the case of SOI-BE we find a value close to that of vacuum. The total inductance L is calculated to be in the range 35–992 nH, while the coil capacitance C is in the range 0.88–7.71 fF. A detailed summary can be found in Table I.

Figure 5 compares the effects of reducing ϵ_{eff} and the pitch on C and Z_C. A reduction of ϵ_{eff} has the effect of decreasing the capacitance, while the inductance remains unchanged, as all substrates have $\mu_r = 1$. We find that C scales linearly with the coil radius $r \simeq np$, in agreement with the expected scaling $C \sim np$ derived earlier. In the limit of a large filling factor $\rho \approx 1$ and $n \gg 1$, the simplification $r = np$ is valid and the self-capacitance of a coil can simply be estimated based on its outer radius for a given substrate, highlighting the importance of miniaturization.

In order to quantify the capacitance suppression, we extract the constant gradient dC/dr for each pitch p and each substrate, resulting in a total of nine data points. The extracted gradients are approximately pitch independent and are therefore averaged for each substrate, resulting in the three values reported in Fig. 5(a). The exception is the SOI substrate, which exhibits a strong pitch dependence (inset), leading to the large 90% confidence interval of ϵ_{eff} reported earlier. The reason is that coils with larger p have a larger size and an electric field distribution with a larger fraction residing in the silicon handle wafer. Moreover, the electric field rapidly decays in the vertical direction, resulting in a large improvement obtained by changing the substrate from silicon to SOI, as can be seen in Figs. 5(a) and 5(b). Simulations suggest that the capacitance suppression saturates for a vacuum gap of around 20 μm, depending on the overall coil size.

The data presented in Fig. 5(b) show the characteristic impedance for measured coils with a similar fundamental frequency $f_0 = (10.7 \pm 0.3)$ GHz. The superlinear improvement obtained by going to lower pitches occurs because fixing the frequency has the effect of approximately fixing the wire length. For a set length, lower-pitch coils have more turns, which gives higher inductance and smaller radii for lower parasitic capacitance. Both have the effect of boosting the characteristic impedance. The dashed lines represent analytical expressions derived from Eqs. (2), (4), and (5) and the bands correspond to the error of ϵ_{eff} as discussed earlier. In the case of SOI, the ϵ_{eff} value is interpolated between different pitches, resulting in a slightly modified shape and a narrow error band.

VI. CONCLUSIONS

In this work, we show that suspended aluminum coils represent linear low-loss geometric superinductor resonators that can be used as an ideal superinductance below their self-resonance frequency. We are able to show

that $Z_C \approx 5 \times R_Q$, about 80 times the previously claimed limitation for geometric inductors, Z_0.

Such a highly miniaturized microwave resonator with large zero-point voltage fluctuations reaching $V_{\mathrm{ZPF}} \approx 50\ \mu\mathrm{V}$, which maintains a linearity of up to 10^8 photons, is an attractive platform for hybrid devices. With losses as low as $Q_i \approx 8 \times 10^5$ at single-photon powers despite the small gap sizes on the order of 100 nm, it will also find applications for new quantum circuits that require a high degree of parameter control and top-down fabrication reproducibility, such as fluxonium and 0-π qubits in new error-protected regimes. Such applications will require a connection to the center of the coil and initial numerical and experimental results confirm that this is possible with low loss and an additional stray capacitance as low as 0.1 fF using the air-bridge process introduced in Refs. [25,45].

Most importantly, and in contrast to circuit elements based on kinetic inductance, the geometric superinductance is a true single-wave-function superconducting device. This rules out the possibility of charge offsets that could impede the visibility of dual Shapiro steps [46], as well as uncontrolled phase- and charge-tunneling events that might become limiting factors for the dephasing times of multiterminal qubits [47,48]. In addition, one can obtain strong magnetic coupling to feed lines or other resonators without significantly increasing the parasitic capacitance, as required for certain error-protected readout and control schemes [15,17].

Our study provides simple analytical models to guide future design choices in such applications. Specifically, we find a simple way to predict the coil self-capacitance that only relies on knowledge of the radius and substrate. Potential challenges include increased flux noise due to the large perimeter of the coil [49], which can be addressed with new materials [50] or improved surface-fabrication techniques. For example, etching rather than lift-off might enable an even smaller coil pitch, with better interfaces and lower TLS losses resulting in even higher values of Z_C. Moreover, we believe that the presented design and fabrication methods could also help to reliably increase the Z_C value of traditional superinductors.

The data and code used to produce the figures in this manuscript are available online [51].

ACKNOWLEDGMENTS

We acknowledge the support from I. Prieto and the Institute of Science and Technology (IST) Nanofabrication Facility (NFF). This work was supported by a NOMIS Foundation research grant, the Austrian Science Fund (FWF) through BeyondC (F71), and IST Austria. M.P. is the recipient of a Pöttinger scholarship at IST Austria. J.M.F. acknowledges support from the European Union's Horizon 2020 research and innovation programs under Grant Agreements No. 732894 (FET Proactive HOT) and No. 862644 (FET Open QUARTET), and from the European Research Council under Grant Agreement No. 758053 (ERC StG QUNNECT).

APPENDIX A: DEVICE FABRICATION

The devices are fabricated on three different substrates, as shown in Figs. 2(a)–2(c). In the case of silicon (Si), the fabrication consists of a single-layer process on a high-resistivity silicon wafer. The coil, ground, and waveguide are patterned by e-beam lithography (EBL) operated at 100 keV on a 300-nm-thick layer of CSAR 13 resist. An evaporation of 100 nm of aluminum at a rate of 1 nm/s in ultrahigh vacuum (UHV) is followed by a lift-off process in *N*-methyl-2-pyrrolidine (NMP) at 80 °C, resulting in the desired metallic pattern.

The fabrication on silicon-on-insulator (SOI) consists of a multilayer fabrication process. The wafer comprises a 220-nm-thick Si layer on 3 μm of silicon dioxide (SiO_2), which rests on 750 μm of Si [45,52]. In the first step, EBL is used to pattern arrays of small holes (radius between 65 and 100 nm depending on the pitch) on the thin Si layer around the coil and on the waveguide. The chip is then mounted in an inductively coupled plasma (ICP) etcher, where C_4F_8 and SF_6 etch the holes through the silicon layer, reaching the oxide, which acts as an etch stop. Then the coil is patterned and evaporated as in the previous case. The last step involves VHF etching (memsstar ORBIS ALPHA), in which the vapor penetrates through the etched holes and locally removes the oxide underneath, thus terminating the process with a suspended membrane.

The last fabrication routine, aimed at producing SOI back-etched (SOI-BE) samples, is developed, deploying a wafer similar to that used in the former procedure, but with the Si handle wafer lapped down to 200 μm. The first two steps are identical to the SOI process, with the difference that in this case no holes are patterned directly around the coils, as they are not needed to suspend the membrane. After the coil-metal deposition and consequent lift-off, a layer of 5 μm of LOR 5B resist is placed on the structures as protection for the following subprocesses. LOR 5B is chosen specifically because it does not dissolve in acetone, used in the next lift-off. A mask is written in EBL on the back side of the chip into 270 nm of PMMA 950k EL4, leaving open rectangles positioned directly under the coil. The rectangles are designed to be large enough for alignment not to be critical. A layer of 50 nm of chromium (Cr) is deposited and the consequent lift-off carried out by acetone at 40 °C. The chip is then mounted in an ICP with the devices facing down and the silicon in the rectangles is completely etched away with a customized Bosh process comprised of a gas mixture of C_4F_8 and SF_6. This leaves only the SiO_2 and 220-nm silicon layer under the coils. For the Cr to stick effectively throughout the etch process, the

bottom of the chip must have a low level of roughness. The resist is then removed via hot NMP and the oxide layer is locally etched by VHF. Finally, the coils are left suspended on a 220-nm membrane with vacuum below.

APPENDIX B: MEASUREMENT AND PARAMETER SUMMARY

The coils are coupled to a shorted waveguide, which guarantees inductive coupling, as shown in Fig. 2(b), where we are able to control the coupling strength by adjusting the distance with a resulting extrinsic quality factor Q_e between 5×10^3 for a distance of a few micrometers and over 10^5 for distances around a couple of times the coil size. Our model does not include parasitic capacitance or mutual inductance due to the coupling wire or the surrounding ground, which in principle can cause small negative and positive shifts in the coil frequency, respectively [53]. Nevertheless, the simulations indicate that these coupling-related shifts are below 1%.

We measure the complex S_{11} parameter using the setup shown in Fig. 2(d) and fit the I and Q quadratures to a reflective model [25] to extract the external and internal quality factors, Q_e and Q_i, and the first resonance frequency, f_0, for all coils as a function of the input power. We are confident that the measured values correspond to the fundamental mode resonance, since the wave-port-coupled FEM simulations of f_0 agree with the data to within 20%. Table I in the main text summarizes the important parameters of all measured devices.

APPENDIX C: TLS AND BCS FIT MODELS

Figure 3(a) in the main text shows the typical dependence of Q_i as a function of the intraresonator photon number n_P, consistent with the presence of TLSs [54]:

$$Q_{\mathrm{TLS}}^{-1} \simeq \frac{F\delta_{\mathrm{TLS}}\tanh(\hbar\omega/2k_{\mathrm{B}}T)}{(1+n_P/n_C)^{\beta}} + Q_{\mathrm{sat}}^{-1}, \tag{C1}$$

where F is the fraction of the electric field in the lossy material, δ_{TLS} is the TLS loss tangent, n_C is the critical photon number that saturates the TLS, and $Q_{\mathrm{sat}} = 1.1 \times 10^6$ represents any additional loss mechanisms. We extract $F\delta_{\mathrm{TLS}}$ to be 1.3×10^{-5}. The exponent β is commonly taken as 0.5 and the deviations indicate an interaction between TLSs [55]. For our system, β is found to be 0.4, which implies some degree of interaction.

In order to quantify the effect of kinetic inductance, we perform temperature sweeps of the same device. Figures 3(b) and 3(c) in the main text show its frequency shift $\delta f\,(T) = f_0(T) - f_0(0)$ and quality-factor degradation $\delta Q_i^{-1}(T) = Q_i^{-1}(T) - Q_i^{-1}(0)$ as a function of the temperature T. This behavior can be accurately modeled using BCS theory [56]:

$$\frac{\delta f\,(T)}{f_0(0)} = -\frac{\alpha\gamma}{2}\frac{\delta\sigma_2(T,\Delta)}{\sigma_2(T,\Delta)} \tag{C2}$$

and

$$\delta Q_i^{-1}(T) = \alpha\gamma\frac{\delta\sigma_1(T,\Delta)}{\sigma_2(T,\Delta)}, \tag{C3}$$

where $\alpha = L_k/(L_g + L_k)$ is the fraction of the kinetic inductance to the total inductance, γ is a material-dependent parameter, which is -1 for aluminum thin films [54], and σ_1 and σ_2 are the real and imaginary parts of the conductance $\sigma = \sigma_1 - i\sigma_2$ as described in Ref. [56]. The data are fitted with α as a free parameter, while the gap voltage Δ is taken to be the bulk value for aluminum, which is shown to be valid for the used film thickness of 100 nm [57]. From the fit, we extract $\alpha = 5.9\%$, which results in a kinetic inductance of $L_k = 58.0$ nH. From this value and $L_k = \mu_0\lambda_L^2(0)(l/wh)$, we infer the London penetration depth $\lambda_L(0) = 147$ nm [44], where μ_0 is the vacuum permeability and l, w, and h are the length, width, and thickness of the wire. The fact that the measured $\lambda_L(0)$ is significantly higher than the value for bulk aluminum (15 nm [54]) is likely due to the thin-film nature of the metal [58].

[1] A. Kitaev, Protected qubit based on a superconducting current mirror, arXiv:cond-mat/0609441 [cond-mat.mes-hall] (2006).

[2] V. E. Manucharyan, Ph.D. thesis, Yale Graduate School of Arts and Sciences, Yale University, 2012.

[3] J. E. Mooij and Y. V. Nazarov, Superconducting nanowires as quantum phase-slip junctions, Nat. Phys. **2**, 169 (2006).

[4] A. Di Marco, F. W. J. Hekking, and G. Rastelli, Quantum phase-slip junction under microwave irradiation, Phys. Rev. B **91**, 184512 (2015).

[5] H. Vora, R. L. Kautz, S. W. Nam, and J. Aumentado, Modeling Bloch oscillations in nanoscale Josephson junctions, Phys. Rev. B **96**, 054505 (2017).

[6] L. Arndt, A. Roy, and F. Hassler, Dual Shapiro steps of a phase-slip junction in the presence of a parasitic capacitance, Phys. Rev. B **98**, 014525 (2018).

[7] K. K. Likharev and A. B. Zorin, Theory of the Bloch-wave oscillations in small Josephson junctions, J. Low Temp. Phys. **59**, 347 (1985).

[8] F. Piquemal and G. Genevés, Argument for a direct realization of the quantum metrological triangle, Metrologia **37**, 207 (2000).

[9] J. Flowers, The route to atomic and quantum standards, Science **306**, 1324 (2004).

[10] V. E. Manucharyan, J. Koch, L. I. Glazman, and M. H. Devoret, Fluxonium: Single Cooper-pair circuit free of charge offsets, Science **326**, 113 (2009).

[11] L. Grünhaupt, M. Spiecker, D. Gusenkova, N. Maleeva, S. T. Skacel, I. Takmakov, F. Valenti, P. Winkel, H.

Rotzinger, W. Wernsdorfer, A. V. Ustinov, and I. M. Pop, Granular aluminium as a superconducting material for high-impedance quantum circuits, Nat. Mater. **18**, 816 (2019).

[12] T. M. Hazard, A. Gyenis, A. Di Paolo, A. T. Asfaw, S. A. Lyon, A. Blais, and A. A. Houck, Nanowire Superinductance Fluxonium Qubit, Phys. Rev. Lett. **122**, 010504 (2019).

[13] B. Douçot and L. B. Ioffe, Physical implementation of protected qubits, Rep. Prog. Phys. **75**, 072001 (2012).

[14] D. T. Le, A. Grimsmo, C. Müller, and T. M. Stace, Doubly nonlinear superconducting qubit, Phys. Rev. A **100**, 062321 (2019).

[15] P. Brooks, A. Kitaev, and J. Preskill, Protected gates for superconducting qubits, Phys. Rev. A **87**, 052306 (2013).

[16] P. Groszkowski, A. D. Paolo, A. L. Grimsmo, A. Blais, D. I. Schuster, A. A. Houck, and J. Koch, Coherence properties of the 0-π qubit, New J. Phys. **20**, 043053 (2018).

[17] A. D. Paolo, A. L. Grimsmo, P. Groszkowski, J. Koch, and A. Blais, Control and coherence time enhancement of the 0-π qubit, New J. Phys. **21**, 043002 (2019).

[18] A. Gyenis, P. S. Mundada, A. D. Paolo, T. M. Hazard, X. You, D. I. Schuster, J. Koch, A. Blais, and A. A. Houck, Experimental realization of an intrinsically error-protected superconducting qubit, arXiv:1910.07542 [quant-ph] (2019).

[19] J. Cohen, W. C. Smith, M. H. Devoret, and M. Mirrahimi, Degeneracy-Preserving Quantum Nondemolition Measurement of Parity-Type Observables for Cat Qubits, Phys. Rev. Lett. **119**, 060503 (2017).

[20] M. Devoret, S. Girvin, and R. Schoelkopf, Circuit-QED: How strong can the coupling between a Josephson junction atom and a transmission line resonator be? Ann. Phys. **16**, 767 (2007).

[21] S. J. Bosman, M. F. Gely, V. Singh, D. Bothner, A. Castellanos-Gomez, and G. A. Steele, Approaching ultra-strong coupling in transmon circuit QED using a high-impedance resonator, Phys. Rev. B **95**, 224515 (2017).

[22] P. Arrangoiz-Arriola, E. A. Wollack, M. Pechal, J. D. Witmer, J. T. Hill, and A. H. Safavi-Naeini, Coupling a Superconducting Quantum Circuit to a Phononic Crystal Defect Cavity, Phys. Rev. X **8**, 031007 (2018).

[23] A. Stockklauser, P. Scarlino, J. V. Koski, S. Gasparinetti, C. K. Andersen, C. Reichl, W. Wegscheider, T. Ihn, K. Ensslin, and A. Wallraff, Strong Coupling Cavity QED with Gate-Defined Double Quantum Dots Enabled by a High Impedance Resonator, Phys. Rev. X **7**, 011030 (2017).

[24] A. Andre, D. DeMille, J. M. Doyle, M. D. Lukin, S. E. Maxwell, P. Rabl, R. Schoelkopf, and P. Zoller, A coherent all-electrical interface between polar molecules and mesoscopic superconducting resonators, Nat. Phys. **2**, 636 (2006).

[25] J. M. Fink, M. Kalaee, A. Pitanti, R. Norte, L. Heinzle, M. Davanço, K. Srinivasan, and O. Painter, Quantum electromechanics on silicon nitride nanomembranes, Nat. Commun. **7**, 12396 (2016).

[26] G. Arnold, M. Wulf, S. Barzanjeh, E. S. Redchenko, A. Rueda, W. J. Hease, F. Hassani, and J. M. Fink, Converting microwave and telecom photons with a silicon photonic nanomechanical interface, Nat. Commun. **11**, 4460 (2020).

[27] G. A. Peterson, S. Kotler, F. Lecocq, K. Cicak, X. Y. Jin, R. W. Simmonds, J. Aumentado, and J. D. Teufel, Ultrastrong Parametric Coupling between a Superconducting Cavity and a Mechanical Resonator, Phys. Rev. Lett. **123**, 247701 (2019).

[28] N. A. Masluk, I. M. Pop, A. Kamal, Z. K. Minev, and M. H. Devoret, Microwave Characterization of Josephson Junction Arrays: Implementing a Low Loss Superinductance, Phys. Rev. Lett. **109**, 137002 (2012).

[29] M. T. Bell, I. A. Sadovskyy, L. B. Ioffe, A. Y. Kitaev, and M. E. Gershenson, Quantum Superinductor with Tunable Nonlinearity, Phys. Rev. Lett. **109**, 137003 (2012).

[30] L. B. Nguyen, Y.-H. Lin, A. Somoroff, R. Mencia, N. Grabon, and V. E. Manucharyan, High-Coherence Fluxonium Qubit, Phys. Rev. X **9**, 041041 (2019).

[31] I. V. Pechenezhskiy, R. A. Mencia, L. B. Nguyen, Y.-H. Lin, and V. E. Manucharyan, The superconducting quasicharge qubit, Nature **585**, 368 (2020).

[32] A. Shearrow, G. Koolstra, S. J. Whiteley, N. Earnest, P. S. Barry, F. J. Heremans, D. D. Awschalom, E. Shirokoff, and D. I. Schuster, Atomic layer deposition of titanium nitride for quantum circuits, Appl. Phys. Lett. **113**, 212601 (2018).

[33] D. Niepce, J. Burnett, and J. Bylander, High Kinetic Inductance NbN Nanowire Superinductors, Phys. Rev. Appl. **11**, 044014 (2019).

[34] S. E. de Graaf, R. Shaikhaidarov, T. Lindström, A. Y. Tzalenchuk, and O. V. Astafiev, Charge control of blockade of Cooper pair tunneling in highly disordered tin nanowires in an inductive environment, Phys. Rev. B **99**, 205115 (2019).

[35] L. Grünhaupt, N. Maleeva, S. T. Skacel, M. Calvo, F. Levy-Bertrand, A. V. Ustinov, H. Rotzinger, A. Monfardini, G. Catelani, and I. M. Pop, Loss Mechanisms and Quasiparticle Dynamics in Superconducting Microwave Resonators Made of Thin-Film Granular Aluminum, Phys. Rev. Lett. **121**, 117001 (2018).

[36] P. Kamenov, W.-S. Lu, K. Kalashnikov, T. DiNapoli, M. T. Bell, and M. E. Gershenson, Granular Aluminum Meandered Superinductors for Quantum Circuits, Phys. Rev. Appl. **13**, 054051 (2020).

[37] D. M. Pozar, *Microwave Engineering* (Wiley, Hoboken, NJ, 2011), 4th ed., p. 54, Chap. 2, Table 2.1.

[38] S. S. Mohan, M. del Mar Hershenson, S. P. Boyd, and T. H. Lee, Simple accurate expressions for planar spiral inductances, IEEE J. Solid-State Circuits **34**, 1419 (1999).

[39] Equation (2) yields accurate results with an error $\leq 8\%$ for thin-film planar circular air-core spiral inductors with $(p - w)/w \leq 3$ in the lumped-element limit [38].

[40] N. Maleeva, A. Averkin, N. N. Abramov, M. V. Fistul, A. Karpov, A. P. Zhuravel, and A. V. Ustinov, Electrodynamics of planar Archimedean spiral resonator, J. Appl. Phys. **118**, 033902 (2015).

[41] An approximated expression of the length of a circular spiral based on a series of concentric circles: $l \simeq \sum_{i=1}^{n} 2\pi r_i \simeq \sum_{i=1}^{n} 2\pi ip = 2\pi(n(n+1)/2)p \simeq n^2 p$.

[42] S. E. Nigg, H. Paik, B. Vlastakis, G. Kirchmair, S. Shankar, L. Frunzio, M. H. Devoret, R. J. Schoelkopf, and S. M. Girvin, Black-Box Superconducting Circuit Quantization, Phys. Rev. Lett. **108**, 240502 (2012).

[43] A. Megrant, C. Neill, R. Barends, B. Chiaro, Y. Chen, L. Feigl, J. Kelly, E. Lucero, M. Mariantoni, P. J. J. O'Malley, D. Sank, A. Vainsencher, J. Wenner, T. C. White, Y. Yin, J. Zhao, C. J. Palmstrøm, J. M. Martinis, and A. N. Cleland, Planar superconducting resonators with internal quality factors above one million, Appl. Phys. Lett. **100**, 113510 (2012).

[44] A. J. Annunziata, D. F. Santavicca, L. Frunzio, G. Catelani, M. J. Rooks, A. Frydman, and D. E. Prober, Tunable superconducting nanoinductors, Nanotechnology **21**, 445202 (2010).

[45] P. B. Dieterle, M. Kalaee, J. M. Fink, and O. Painter, Superconducting Cavity Electromechanics on a Silicon-on-Insulator Platform, Phys. Rev. Appl. **6**, 014013 (2016).

[46] K. Cedergren, R. Ackroyd, S. Kafanov, N. Vogt, A. Shnirman, and T. Duty, Insulating Josephson Junction Chains as Pinned Luttinger Liquids, Phys. Rev. Lett. **119**, 167701 (2017).

[47] A. Mizel and Y. Yanay, Right-sizing fluxonium against charge noise, Phys. Rev. B **102**, 014512 (2020).

[48] A. Di Paolo, T. E. Baker, A. Foley, D. Sénéchal, and A. Blais, Efficient modeling of superconducting quantum circuits with tensor networks, arXiv:1912.01018 [quant-ph] (2019).

[49] J. Braumüller, L. Ding, A. P. Vepsäläinen, Y. Sung, M. Kjaergaard, T. Menke, R. Winik, D. Kim, B. M. Niedzielski, A. Melville, J. L. Yoder, C. F. Hirjibehedin, T. P. Orlando, S. Gustavsson, and W. D. Oliver, Characterizing and Optimizing Qubit Coherence Based on SQUID Geometry, Phys. Rev. Appl. **13**, 054079 (2020).

[50] A. P. M. Place, L. V. H. Rodgers, P. Mundada, B. M. Smitham, M. Fitzpatrick, Z. Leng, A. Premkumar, J. Bryon, S. Sussman, G. Cheng, T. Madhavan, H. K. Babla, B. Jaeck, A. Gyenis, N. Yao, R. J. Cava, N. P. de Leon, and A. A. Houck, New material platform for superconducting transmon qubits with coherence times exceeding 0.3 milliseconds, arXiv:2003.00024 [quant-ph] (2020).

[51] M. Peruzzo, A. Trioni, F. Hassani, M. Zemlicka, and J. M. Fink, Data for: Surpassing the Resistance Quantum with a Geometric Superinductor, (2020) https://doi.org/10.5281/zenodo.4052883.

[52] A. J. Keller, P. B. Dieterle, M. Fang, B. Berger, J. M. Fink, and O. Painter, Al transmon qubits on silicon-on-insulator for quantum device integration, Appl. Phys. Lett. **111**, 042603 (2017).

[53] J. W. Hooker, V. Ramaswamy, R. K. Arora, A. S. Edison, and W. W. Brey, Effects of dielectric substrates and ground planes on resonance frequency of Archimedean spirals, IEEE Trans. Appl. Supercond. **26**, 1 (2016).

[54] J. Gao, Ph.D. thesis, Division of Engineering and Applied Science, California Institute of Technology, 2008.

[55] J. Burnett, J. Sagar, O. W. Kennedy, P. A. Warburton, and J. C. Fenton, Low-Loss Superconducting Nanowire Circuits Using a Neon Focused ion Beam, Phys. Rev. Appl. **8**, 014039 (2017).

[56] J. Gao, J. Zmuidzinas, A. Vayonakis, P. Day, B. Mazin, and H. Leduc, Equivalence of the effects on the complex conductivity of superconductor due to temperature change and external pair breaking, J. Low Temp. Phys. **151**, 557 (2008).

[57] P. N. Chubov, V. V. Eremenko, and Y. A. Pilipenko, Dependence of the critical temperature and energy gap on the thickness of superconducting aluminum films, Sov. Phys. JETP **28**, 389 (1969).

[58] C. Reale, Thickness and temperature dependence of the critical magnetic field of thin superconducting films of the aluminium group metals, Acta Phys. **37**, 53 (1974).